WARSAW UNIVERSITY OF TECHNOLOGY Index 351733
FACULTY OF CIVIL ENGINEERING
COMMITTEE FOR CIVIL AND WATER ENGINEERING
POLISH ACADEMY OF SCIENCES ISSN 1230-2945
DOI: 10.24425/ace.2024.149861
ARCHIVES OF CIVIL ENGINEERING
Vol. LXX ISSUE 2 2024
pp. 233 –254

Research paper

Conventional triaxial loading and unloading test and PFC numerical simulation of rock with single fracture

Yin Tang[1], Haijun Chen[2], Liangxiao Xiong[3], Zhongyuan Xu[4]

Abstract: Take the metamorphic sandstone as the reference object, by making rock like samples with fractures, the conventional triaxial loading and unloading test and PFC numerical simulation of rock like sample with single fracture were conducted, and the effects of the loading path, inclined angle of fracture, axial stress level during unloading, initial confining pressure during unloading on the compressive strength, peak strain and crack propagation evolution of the samples were considered. The compressive strength of the specimen under triaxial unloading is smaller than that under triaxial loading. The peak strain of the specimen under triaxial unloading is also smaller than that under triaxial loading. The specimen is more prone to brittle failure. When the axial stress level is the same during unloading, with the increase of the initial confining pressure during unloading, the difference of the compressive strength of the specimens with different inclined angles of fracture gradually decreases. Under the condition of uniaxial compression and triaxial compression, the failure of all specimens is tensile failure, and the shear failure is the main one during unloading.

Keywords: rock like specimen, triaxial loading and unloading test, compressive strength

[1]Eng., Geotechnical Engineering Institute, Sichuan Institute of Building Research, Chengdu 610081, China, e-mail: 18428322238@163.com, ORCID: 0009-0008-1831-1532
[2]Prof., PhD., Eng., Geotechnical Engineering Department, Nanjing Hydraulic Research Institute, Nanjing, 210029, China, e-mail: hjchen@nhri.cn, ORCID: 0000-0003-0094-9649
[3]Associate Prof., PhD., Eng., School of Civil Engineering and Architecture, East China Jiaotong University, Nanchang 330013, China, e-mail: xionglx1982@126.com, ORCID: 0000-0002-6366-5187
[4]PhD, Faculty of Geosciences and Environmental Engineering, Southwest Jiaotong University, Chengdu 611756, China, e-mail: zyxu@swjtu.edu.cn, ORCID: 0000-0003-4303-1870

1. Introduction

In actual tunnel engineering, because of the loading and unloading of stress of surrounding rock caused by excavation, the study of mechanical properties of rock under loading and unloading conditions has always been the focus of rock mechanics.

Chen *et al*. [1] analyzed and compared rock salt dilatancy behaviors under triaxial unloading confining pressure tests with those from conventional uniaxial and triaxial compression tests, and found that the volume deformation of rock salt under unloading is more than under triaxial loading, but less than under uniaxial loading. Guo *et al*. [2] studied the effects of different bedding angles and mineral compositions on the mechanical properties and failure modes of phyllites under unloading confining pressure conditions, and found that the deformation characteristics of phyllite have complex relations with confining pressure, bedding angle and mineral composition. Chen *et al*. [3] analyzed the mechanical properties of Beizao sandstone specimens under conventional triaxial compression and triaxial loading and unloading compression conditions, and found that the strain-softening modulus of the sandstone specimens under triaxial loading and unloading compression conditions decreased with the increases in the loading rate. Dai *et al*. [4] performed a series of conventional tri-axial compression tests on specimens to investigate the damage characteristics of rocks in loading and unloading, and found that the failure strain for unloading is smaller than that for loading under all three confining pressures. Dai *et al*. [5] investigated the damage evolution characteristics of a granitic rock during loading and unloading after a series of triaxial experiments performed at different confining pressures, and found that specimens under pure loading failed with a single distinct shear fracture while for the unloading case specimens displayed multiple intersecting fractures. Chen *et al*. [6] conducted a series of laboratory tests in order to investigate the effects on crack propagation characteristics of confining pressure, as well as the effect of the unloading rates of confining pressure, and found that with increases in the unloading rates of the confining pressure, increases will occur in the crack volumetric propagation strain and crack propagation velocity of the sandstone. Huang *et al*. [7] carried out triaxial unloading confining pressure tests on sandy mudstone specimens to study the dilatancy and fracturing behavior of soft rock, and found that when the unloading rate is smooth the peak strengths and deviatoric stress-strain curves under the unloading condition are close to those under the conventional loading condition. Li *et al*. [8] conducted loading and unloading tests with various confining pressures to investigate the mechanical properties of marble material samples, and found that in the loading and unloading test, peak strength, lateral strain, axial strain and plastic deformation increase significantly as the confining pressure increases. An *et al*. [9] analyzed the evolution of the pre-peak strain energy of diorite under triaxial loading and unloading paths using laboratory tests and numerical simulations. They found that the ultimate strain energy accumulation capacity of diorite increased with the timing of unloading confining pressure and axial loading rate, while it decreased with the unloading confining pressure rate. Dai *et al*. [10] explored the damage and deformation characteristics of salt rock under triaxial cyclic loading and unloading. They discovered that the growth rate of elastic energy and dissipated energy increased gradually with the increase of deviatoric

stress. Gong *et al*. [11] conducted triaxial loading and unloading tests of fractured rock samples with different dip angles under different stress paths. The results showed that failure modes of fractured granite under triaxial loading and unloading are primarily dominated by shear failure. Meng *et al*. [12] carried out triaxial cyclic loading and unloading test of rock specimens under 6 confining pressures. They noted that the rock specimen strength increased as the confining pressure increased. Yin *et al*. [13] conducted experiments and simulations to investigate the mechanical response and mechanism of shale specimens under cyclic loading and unloading, and found that the unloading modulus was greater than the loading modulus in each cycle.

The above literature studies the triaxial unloading mechanical properties of intact rock. There are often cracks in actual rock mass engineering, so it is more suitable to study the triaxial loading and unloading mechanical characteristics of rock with cracks. Li *et al*. [14] simulated the unloading process of pre-flawed rock material by distinct element method, and the results indicate that the unloading failure strength of pre-flawed specimen exhibits a power-function increase trend with the increase of unloading period.

Therefore, the test results of triaxial loading and unloading mechanical properties of rock with cracks have not been reported in literature. In this paper, taking the metamorphic sandstone as the reference object, through making rock like samples with cracks, the mechanical properties of the samples under conventional triaxial loading and unloading are tested, and the effects of loading path, crack inclination, axial stress level during unloading, and initial confining pressure during unloading on the compressive strength, peak strain and crack propagation evolution of the specimens are studied.

2. Test scheme

2.1. Sample preparation

Taking the metamorphic sandstone of the deep long tunnel as the reference object, cement, barite powder, water, polycarboxylic acid superplasticizer, etc. are used to make rock like specimens. When the density, uniaxial compressive strength, cohesion and internal friction angle of intact rock like specimen are close to the corresponding physical parameters of metamorphic sandstone, the final mix ratio of similar materials tested by orthogonal design shall be determined to continue to make intact rock samples and rock samples with single fracture.

425 Portland cement were used as the cement and medium standard sand were used as the sand when making the sample. The specimen is a cylindrical specimen with a diameter of 50 mm and a height of 100 mm. Finally, it is determined that the mass of cement, barite powder, sand, water and water reducer is 3.17 kg, 1.90 kg, 2.86 kg, 1.59 kg and 0.48 kg, respectively for every 10 kg of the complex. The comparison of physical and mechanical parameter values of metamorphic sandstone and rock like samples are shown in Table 1.

Weigh the raw and dry materials required for the experiment according to the pre-determined ratio and ensure a thorough mix. Added the measured water and water-reducing

Table 1. Comparison of physical and mechanical parameters of metamorphic sandstone and rock like samples

Rock sample type	density (g/cm^3)	compressive strength (MPa)	cohesion (MPa)	internal friction angle (°)
Metamorphic sandstone	2.71	49.97~68.6	14.61	33.6
Rock like	1.87	32.45	7.87	31.02

agent, and quickly mix them with a mixer for 3 minutes. Subsequently, pour the mixture into the mold as shown in Fig. 1, and vibrate for one minute. Then pull out the PVC film after 12 hours to form an empty crack in the sample, as shown in Fig. 2. The PVC film, approximately 2mm thick, runs throughout the entire mold, forming the crack that traverses the specimen. In this study, the advantage of using rock like specifications is that it is convenient to make rock samples containing cracks, but the disadvantage is that the physical and mechanical parameters of the samples differ from those of the metallic sandstone.

Fig. 1. Mold for making sandstone like samples with cracks

Fig. 2. Rock like specimen

2.2. Fracture combination form

The length of cracks in all samples is 20 mm and the thickness is about 2 mm. Inclined angle β of prefabricated crack is the angle between the prefabricated crack and the horizontal line, and the inclined angle β includes 5 kinds, i.e. 0°, 30°, 45°, 60° and 90°. Inclined angle β of prefabricated crack in the specimen is as shown in Fig. 3.

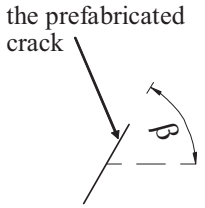

Fig. 3. Schematic diagram of inclined angle β of prefabricated crack in the specimen

2.3. Test grouping

The tests carried out in this paper include triaxial compression loading test and triaxial compression unloading test. The inclined angle β includes 5 kinds, i.e. 0°, 30°, 45°, 60° and 90°, and the confining pressure includes 0 MPa, 5 MPa, 10 MPa and 15 MPa when conducting triaxial compression loading test. The inclined angle β includes 5 kinds, i.e. 0°, 30°, 45°, 60° and 90°, and the initial confining pressure at unloading is 10 MPa when conducting triaxial compression unloading test.

Loading steps of triaxial compression test: firstly, increase the confining pressure to the preset value at the loading rate of 0.5 MPg/s, stabilize the pressure for 15 s, and then continue to apply the axial pressure at 1 kN/s until the specimen is damaged.

Loading steps of triaxial unloading test: firstly, increase the confining pressure to the preset value at the loading rate of 0.5 MPa/s, stabilize the pressure for 15 s, continue to apply the axial pressure to a certain axial stress value before the specimen is destroyed (take 70% of the corresponding conventional triaxial compressive strength), and then increase the axial pressure and unloading the confining pressure at the same rate of 0.05 MPa/s until the specimen is destroyed.

3. Analysis of test results of mechanical characteristics of triaxial loading and unloading

3.1. Analysis of test results of mechanical properties under conventional triaxial loading

The stress-strain curves of specimen of uniaxial compression test are shown in Fig. 4.

When the inclined angle β is 0°, 30°, 45°, 60° and 90°, the compressive strength of the specimen is 13.91, 14.72, 21.10, 20.79 and 26.91 MPa, respectively. The compressive strength of the intact specimen is 33.69 MPa.

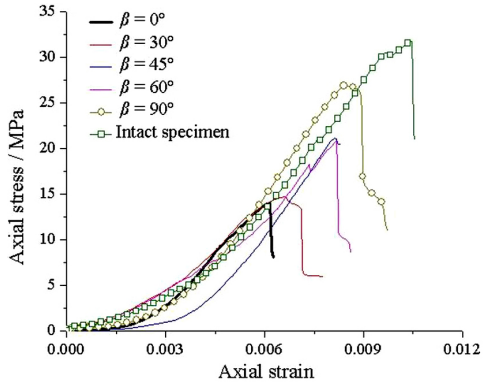

Fig. 4. Stress-strain curve of specimen of uniaxial compression test

When the confining pressure is 10 MPa, and the inclined angle β is 0°, 30°, 45°, 60° and 90°, the stress-strain curves of the triaxial compression test of the specimen are shown in Fig. 5.

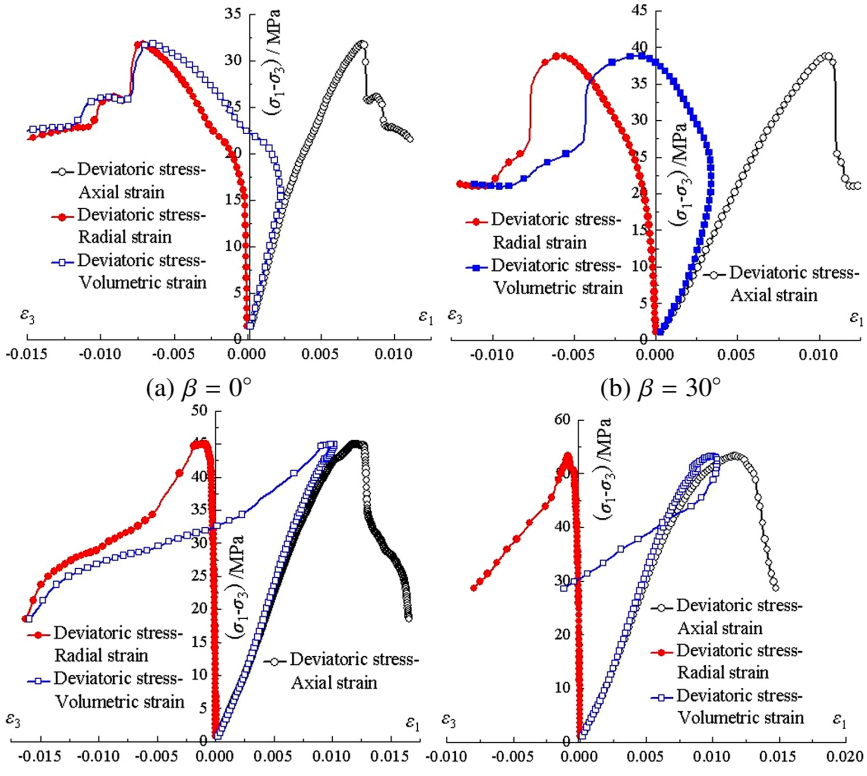

(a) β = 0° (b) β = 30°

(c) β = 45° (d) β = 60°

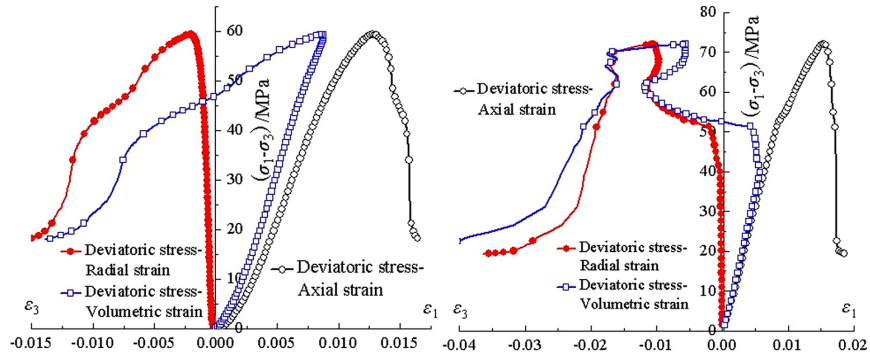

(e) $\beta = 90°$ (f) intact specimen

Fig. 5. Triaxial compression test curves of specimens with cracks with different inclined angles

At the initial stage of the elastic stage, the curves of the deviator stress-axial strain and the deviator stress – volume strain almost coincide. With the radial deformation of the specimen, the deviator stress volume strain changes from positive to negative, and volume expansion occurs.

Both the specimen with cracks and the intact specimen have dilatancy.

The post peak stress-strain curve of the specimen with inclined angle of 0° has an obvious step drop, which indicates that the crack is still expanding after the specimen is destroyed. The post peak stress-strain curves of the specimens with inclined angles of 30°, 45°, 60° and 90° and the intact specimens all decrease linearly. With the inclined angle β of prefabricated crack increasing from 0° to 90°, the compressive strength of the specimen also gradually increases. Under the same confining pressure, the compressive strength of the intact specimen is greater than that of the specimen with cracks.

The deviator stress-axial strain curve of the specimen with inclined angle of 45° under different confining pressures is shown in Fig. 6.

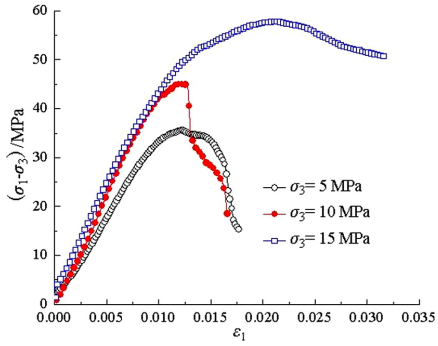

Fig. 6. Deviator stress-strain curves of specimens with fracture inclination of 45° under different confining pressures

When the confining pressure is 5 MPa, 10 MPa and 15 MPa, the deviator stress of the specimen with inclined angle of 45° is 35.56 MPa, 45.37 MPa and 57.77 MPa, respectively. Therefore, the compressive strength of the specimen increases with the increase of confining pressure. When the confining pressure is 5 MPa and 10 MPa, the post peak deviator stress-axial strain curve of the specimen drops rapidly. When the confining pressure is 15 MPa, the post peak deviator stress-axial strain curve of the specimen decreases slowly and the plasticity increases obviously. Therefore, the confining pressure has an obvious effect on the failure mode of the specimen.

3.2. Analysis of test results of triaxial unloading mechanical characteristics

The confining pressure is 10 MPa, and the inclined angle $\beta$of prefabricated crack is 0°, 30°, 45°, 60° and 90°, the comparison of stress-strain curves of triaxial unloading test and triaxial loading test of specimen is shown in Fig. 7.

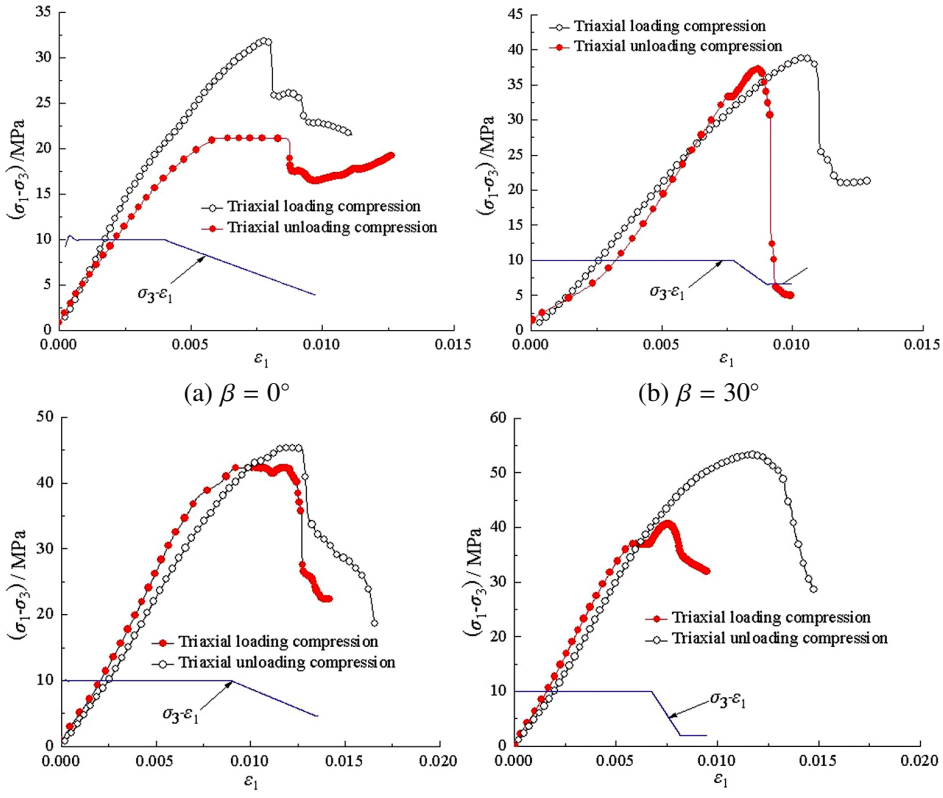

(a) β = 0° (b) β = 30°

(c) β = 45° (d) β = 60°

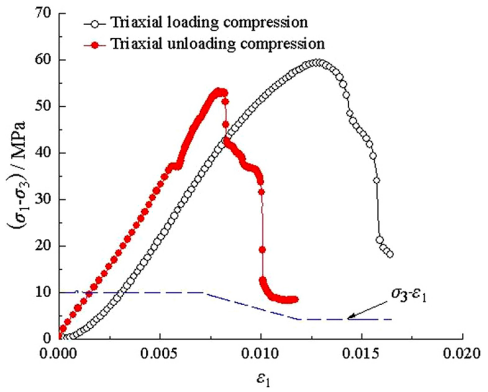

(e) $\beta = 90°$

Fig. 7. Comparison of stress-strain curves between triaxial unloading test and triaxial loading test

The compressive strength of the specimen under triaxial unloading is smaller than that under triaxial loading. The peak strain corresponding to the peak stress of the specimen under triaxial unloading is also smaller than that under triaxial loading. The specimen is more prone to brittle failure. When the specimen with inclined angle of 0° is unloaded, the deviator stress after the peak decreases first and then increases with the unloading process. For the samples with inclined angle of 30–90°, the deviator stress after the peak decreases gradually with the unloading, and there is no obvious plastic platform. For the specimen with inclined angle of 0–90°, the plastic platform appears in the deviator stress-axial strain curve of the specimen near the initial unloading point.

When the confining pressure is 10 MPa, and the inclined angle β of prefabricated crack is 45°, the relationship curves of deviator stress-axial strain, deviator stress-radial strain and deviator stress-volume strain of the specimen under triaxial loading and triaxial unloading are shown in Fig. 8.

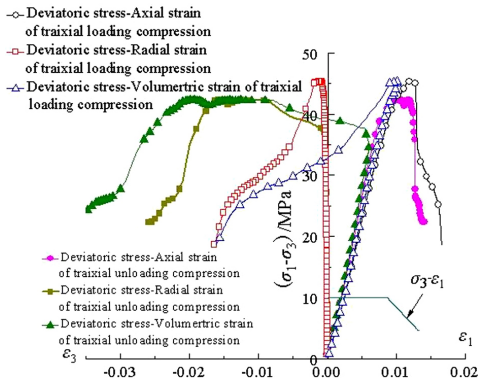

Fig. 8. Comparison of various deviator stress-strain curves under triaxial loading and triaxial unloading when the inclined angle β of prefabricated crack is 45°

During the initial stage of triaxial loading test and triaxial unloading test, the deviator stress-axial strain curve and the deviator stress-volume strain curve almost coincide with each other. When the triaxial unloading test is carried out, the radial strain begins to increase sharply near the initial unloading point, and the deviator stress-volume strain curve changes from positive value to negative value. The volume expansion of the specimen after the triaxial unloading test is earlier than that after the triaxial loading test. The volume expansion of the specimen after the triaxial unloading test is greater than that after the triaxial loading test. The compressive strength of the specimen under triaxial unloading test is obviously less than that under triaxial loading test.

3.3. Analysis of crack evolution results during triaxial loading and unloading mechanical test

The fracture diagram of the specimen during uniaxial compression test is shown in Fig. 9.

(a) $\beta = 0°$ (b) $\beta = 30°$ (c) $\beta = 45°$ (d) $\beta = 60°$ (e) $\beta = 90°$ (f) Intact specimen

Fig. 9. Fracture diagram of specimen during uniaxial compression test

Under the condition of uniaxial compression, the failure of the specimen is mainly caused by the propagation and penetration of the wing crack and the secondary crack at the tip of the preformed crack. The mode of crack generation and penetration is different when the inclined angle of prefabricated crack is different. When the inclined angle of the prefabricated crack is 0°, there are obvious wing tensile cracks and secondary cracks in the specimen. With the increase of the axial stress, the wing cracks and secondary cracks gradually extend to the loading end, causing the specimen to undergo macro damage. When the inclined angle of the prefabricated crack is 30°, the failure mode of the specimen is similar to that with inclined angle of the prefabricated crack of 0°, and the continuous expansion of the secondary crack and the wing crack also leads to the fracture of the specimen. When the inclined angle of the prefabricated crack is 45°, the cracks of the specimen increase obviously during the failure, and the crack branches are generated in the secondary cracks, and the cracks expand along the direction of the prefabricated crack to form tensile splitting. When the inclined angle of the prefabricated crack is 60°, there is a shear crack on the top of the specimen, and it is also the crack propagation at the tip of the

prefabricated crack that leads to the tensile splitting failure. When the inclined angle of the prefabricated crack is 90°, the tensile crack is formed along the direction of the prefabricated crack, and the specimen has been destroyed and lost its bearing capacity when the crack is not completely penetrated. The intact specimen is destroyed due to the formation of macro shear fracture surface in the specimen.

The fracture diagram of the specimen under triaxial compression with confining pressure of 10 MPa is shown in Fig. 10, and the sketch diagram of the specimen under triaxial compression with confining pressure of 10 MPa is shown in Fig. 11.

(a) $\beta = 0°$ (b) $\beta = 30°$ (c) $\beta = 45°$ (d) $\beta = 60°$ (e) $\beta = 90°$ (f) Intact specimen

Fig. 10. Fracture diagram of specimen under triaxial compression with confining pressure of 10 MPa

(a) $\beta = 0°$ (b) $\beta = 30°$ (c) $\beta = 45°$ (d) $\beta = 60°$ (e) $\beta = 90°$ (f) Intact specimen

Fig. 11. Sketch of specimen fracture under triaxial compression with confining pressure of 10 MPa

When the inclined angle β of fracture dip angle is 0°, the crack propagation direction is parallel to the direction of the maximum principal stress, and its failure mode is similar to that of the intact specimen, which is tensile failure. When the inclined angle β of fracture dip angle is 30°, the tip of the prefabricated crack has an wing tensile crack, and the tip of the prefabricated crack also has a shear crack. The tensile crack parallel to the direction of the maximum principal stress penetrates, which belongs to the tensile shear composite

failure. When the inclined angle β of fracture dip angle is 45°, the tensile crack at the tip of the preformed crack expands obviously, and the failure of the specimen is mainly caused by tensile splitting. When the inclined angle β of fracture dip angle is 60°, the specimen produces shear failure along the prefabricated crack, and tensile crack appears at the tip of the prefabricated crack. When the inclined angle β of fracture dip angle is 90°, the macro fracture surface is formed along the direction of the prefabricated crack, and the tensile failure of the specimen occurs.

The fracture diagram of the specimen under triaxial unloading with confining pressure of 10 MPa is shown in Fig. 12, and the sketch diagram of the specimen under triaxial unloading with confining pressure of 10 MPa is shown in Fig. 13.

(a) $\beta = 0°$ (b) $\beta = 30°$ (c) $\beta = 45°$ (d) $\beta = 60°$ (e) $\beta = 90°$ (f) Intact specimen

Fig. 12. Fracture diagram of specimen under triaxial unloading with confining pressure of 10 MPa

(a) $\beta = 0°$ (b) $\beta = 30°$ (c) $\beta = 45°$ (d) $\beta = 60°$ (e) $\beta = 90°$ (f) Intact specimen

Fig. 13. Sketch of specimen fracture under triaxial unloading with confining pressure of 10 MPa

When the inclined angle β of fracture dip angle is 0°, the shear failure of the specimen mainly occurs along the crack surface under unloading, and the tip of the prefabricated crack also produces wing tensile crack. When the inclined angle β of fracture dip angle is

30°, the wing crack at the tip of the preformed crack propagates and penetrates, and the shear failure of the specimen occurs. When the inclined angle β of fracture dip angle is 45°, coplanar secondary cracks are formed at the tip of the prefabricated crack, and the secondary cracks extend and penetrate along the direction of the prefabricated crack to form a shear plane. At the tip of the prefabricated crack, there are also wing tensile cracks, and the specimen is mainly subjected to tensile shear failure. When the inclined angle β of fracture dip angle is 60°, the shear crack also exists at the tip of the prefabricated crack. When the inclined angle β of fracture dip angle is 90°, the macro fracture surface is formed along the direction of the preformed crack, and the tensile failure occurs in the specimen, which is the same as that of the conventional triaxial loading specimen.

Two groups of shear planes are formed in the intact specimen, and the shear planes are nearly parallel. The shear failure plane is connected by other failure planes, and a diagonal fracture plane is formed in the specimen.

4. Determination of numerical simulation parameters

The fish language provided by PFC^{2D} program is used to establish the numerical simulation calculation model of rock with cracks. Due to the fact that cracks penetrate the specimen, it is feasible to use 2D numerical simulation. Establish a 50 mm (diameter) ×100 mm (high) numerical model based on the relevant physical parameters of the intact test specimen. The particles are uniformly distributed, the particle size is 0.6–0.9 mm, the particle density is 2700 kg/m^3, and the porosity is 0.08. 2566 spheres are generated in the complete sample, and the generated particles are constrained by 4 boundary walls. After the intact model is generated, the side walls and particles outside the size are deleted. Simulating the experimental results outlined in Sections 3.1 and 3.2 involves continuous adjustments to the micro parameters. The micro parameters are determined once the numerical simulation results align closely with the experimental findings. The mesoscopic parameters of the intact specimen are shown in Table 2.

Table 2. Meso parameters of an intact specimen

Particle contact Modulus / GPa	Particle normal-tangential stiffness ratio	Particle friction coefficient	Particle density kg/m^3	Porosity	Parallel bonding average Normal strength / MPa	Parallel bonding average tangential strength / MPa
5.4	1.5	0.3	2700	0.08	28.14	13.6

Utilize the PFC built-in Fish language to program routine mechanical loading and unloading, achieving simulation experiments of loading and unloading by controlling the movement of the wall. In the simulation of uniaxial compression tests, the lateral pressure servo loading can be turned off, and the axial pressure loading program can be activated to

load by controlling the displacement of the top and bottom walls. During the simulation of triaxial loading and conventional loading and unloading tests, open the lateral pressure loading servo program, first apply lateral stress to the preset value, then activate the axial pressure servo, and control the application of confining pressure on the left and right walls to ensure alignment with indoor testing methods. In the simulation of three-axis unloading, control the axial pressure to the preset value, then close the confining pressure servo program. Subsequently, activate the lateral unloading program, unloading while the axial pressure continues to increase.

The comparison between the test results and the numerical simulation results of the triaxial compression stress-strain curve of the intact specimen is shown in Fig. 14, and the comparison between the test results and the numerical simulation results of the failure mode is shown in Fig. 5.

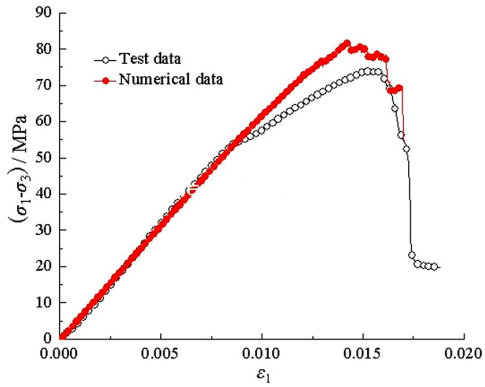

Fig. 14. Comparison of test results and numerical simulation results of triaxial compression stress-strain curves of intact specimens

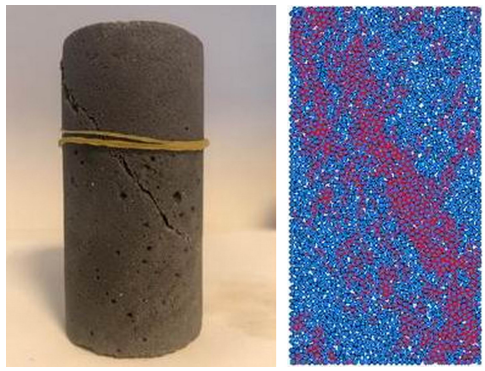

(a) Test results (b) numerical simulation results

Fig. 15. Comparison of test results and numerical simulation results of triaxial compression fracture mode of intact specimens

When the confining pressure is 10 MPa, the triaxial compressive strength and elastic modulus of the specimen obtained from the test are 72.16 MPa and 8.66 GPa, respectively. The triaxial compressive strength and elastic modulus of the sample obtained from the numerical simulation are 82.04 MPa and 8.72 GPa, respectively. It can be seen from Figure 14 and Figure 15 that the numerical simulation results are in good agreement with the test results. Therefore, the established numerical model and meso parameters can be used to furtherly carry out the meso numerical simulation of the triaxial loading and unloading mechanical characteristics of the specimen with cracks.

5. Analysis of numerical simulation results of triaxial compression loading and unloading

5.1. Numerical simulation analysis of triaxial compression test results

The numerical simulation results of the uniaxial compression stress-strain curve of the specimen are shown in Fig. 16.

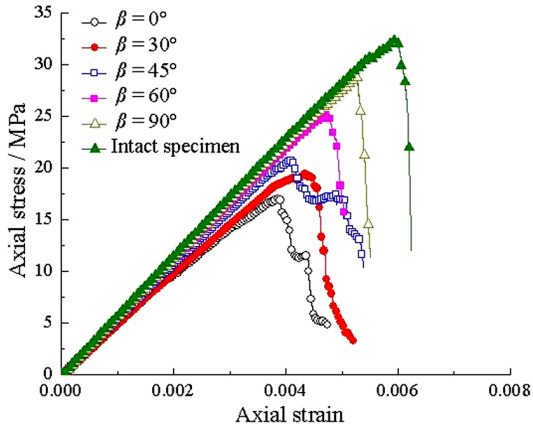

Fig. 16. Numerical simulation results of uniaxial compressive stress-strain curves of the specimens

When the inclined angle $\beta$of prefabricated crack increasing from 0° to 90°, the compressive strength and peak strain of the specimen increase gradually. The compressive strength of the intact specimen is the largest and is 32.3 MPa.

When the confining pressure is 5 MPa, 10 MPa and 15 MPa, the triaxial compressive stress-strain curve of the specimen is shown in Fig. 17.

When the inclined angle $\beta$of the prefabricated crack is the same, with the increase of confining pressure, the triaxial compressive strength of the specimen increases gradually.

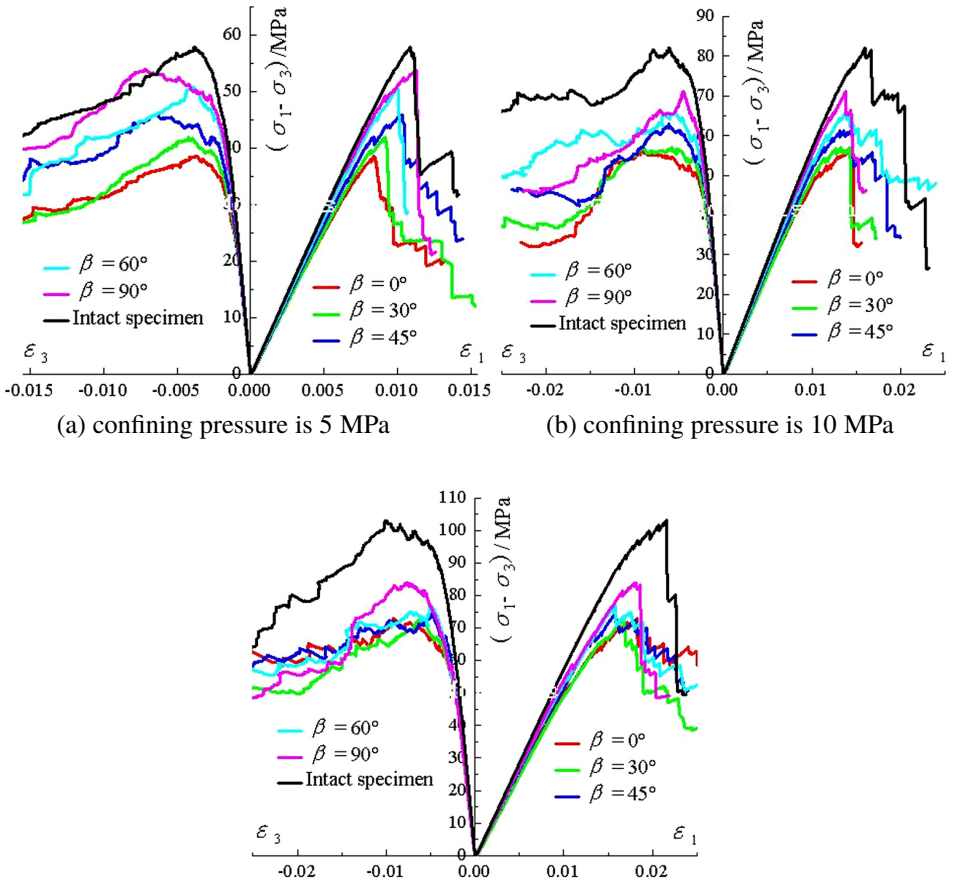

(a) confining pressure is 5 MPa

(b) confining pressure is 10 MPa

(c) confining pressure is 15 MPa

Fig. 17. Numerical simulation results of triaxial compression stress-strain curves of specimens

5.2. Numerical simulation analysis of triaxial compression unloading test results

When the confining pressure is 5 MPa, 10 MPa and 15 MPa, the initial axial stress level at the time of unloading is 70% of the corresponding conventional triaxial compressive strength, the deviator stress-axial strain relationship curve at the time of unloading is shown in Fig. 18. When the confining pressure is 10 MPa, the initial axial stress level at the time of unloading is 60% and 80% of the corresponding conventional triaxial compressive strength, the deviator stress-axial strain relationship curve of unloading is shown in Fig. 19.

When the initial confining pressure at unloading is the same, the axial stress level at unloading is the same, and the inclined angle $\beta$of prefabricated crack increasing from 0° to 90°, the strength of the specimen at unloading also gradually increases. When the initial confining pressure at unloading is the same and the inclined angle $\beta$of prefabricated crack

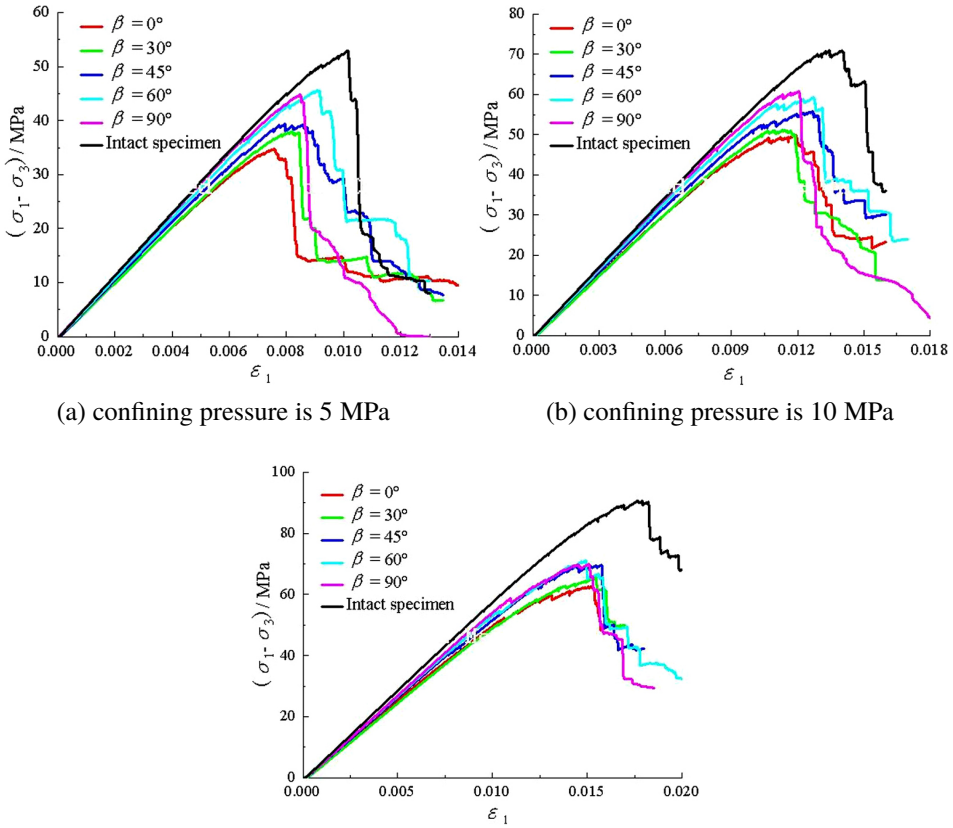

(a) confining pressure is 5 MPa

(b) confining pressure is 10 MPa

(c) confining pressure is 15 MPa

Fig. 18. Numerical simulation results of triaxial unloading stress-strain curves of specimens at confining pressures of 5 MPa, 10 MPa and 15 MPa

is the same, with the increase of the axial stress level during unloading, the strength of the specimen during unloading also gradually increases. When the axial stress level is the same during unloading, with the increase of the initial confining pressure during unloading, the difference of the compressive strength of the specimens with different fracture angles gradually decreases.

When the inclined angle $\beta$of prefabricated crack is 45° and the initial confining pressure at unloading is 5 MPa, 10 MPa and 15 MPa, respectively, the deviator stress-axial strain relationship curves are shown in Fig. 20.

It can be seen from Figure 20 that when inclined angle βin the sample is the same, the compressive strength of the conventional triaxial compression test is significantly greater than that of the triaxial unloading, which is the same as the results obtained from the test.

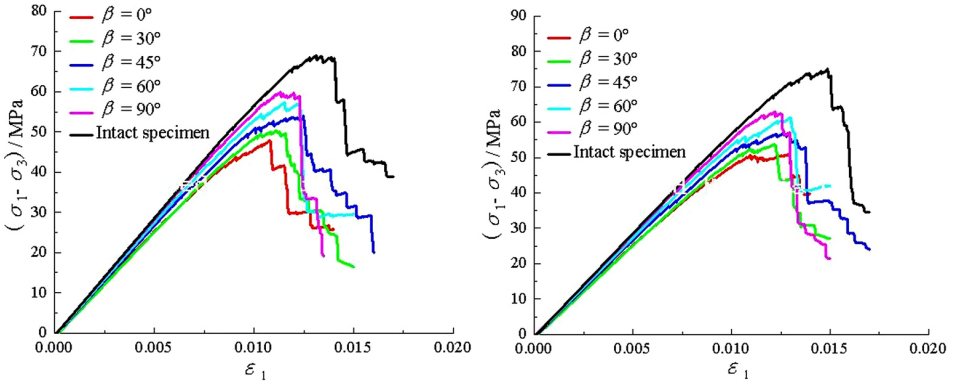

(a) 60% (b) 80%

Fig. 19. When unloading, the initial axial stress level is 60% and 80% of the corresponding conventional triaxial compressive strength

5.3. Numerical simulation results of crack evolution during triaxial loading and unloading mechanical test

The numerical simulation results of the triaxial compression fracture of the specimen at confining pressures of 10 MPa and 15 MPa are shown in Fig. 21 and Fig. 22.

In Fig. 21 and Fig. 22, the red broken line represents the tension crack, the blue broken line represents the tension shear crack, and the green broken line represents the compression shear crack.

The intact specimen begins to produce cracks along the symmetry angle direction of the specimen. The cracks first appear on the top of the specimen, and tensile cracks occur along the fracture direction, accompanied by shear cracks. With increased confining pressure, the tensile shear cracks decrease, and the compressive shear cracks gradually increase. The specimens with prefabricated cracks start to generate shear cracks at both ends of the prefabricated cracks, germinate and expand to the symmetry angle of the specimens, and finally form a macro fracture surface. When the specimens reach the compressive strength, symmetrical shear cracks will be associated on both sides of the main fracture direction. The internal of the specimens with prefabricated cracks is mainly compression shear failure. When the inclined angle of prefabricated crack is 90°, the wing crack and the secondary crack begin to appear from both ends of the prefabricated crack, and develop through to form a macro fracture surface, which is close to the results of the laboratory test.

When the confining pressure is 10 MPa and 15 MPa, the initial axial stress level during unloading is 70% of the corresponding conventional triaxial compressive strength, the numerical simulation results of the triaxial unloading fracture of the specimen are shown in Fig. 23 and Fig. 24. When the confining pressure is 10 MPa, the initial axial stress level during unloading is 80% of the corresponding conventional triaxial compressive strength, the numerical simulation results of the triaxial unloading fracture of the specimen are shown in Fig. 25.

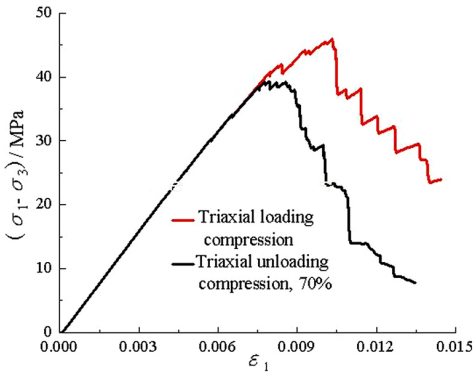

(a) confining pressure is 5 MPa

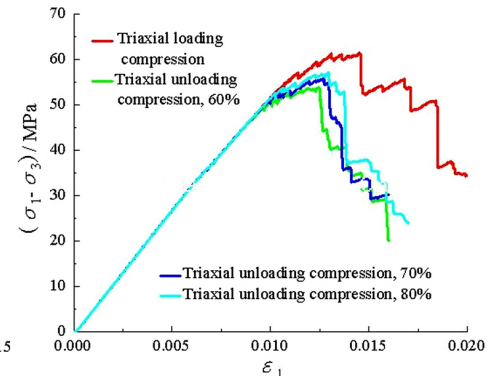

(b) confining pressure is 10 MPa

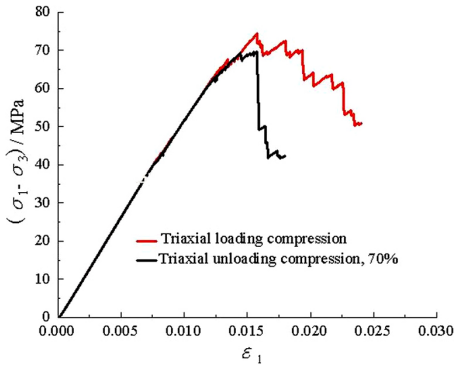

(c) confining pressure is 15 MPa

Fig. 20. Numerical simulation results of triaxial unloading stress-strain curve of the specimen at 45°

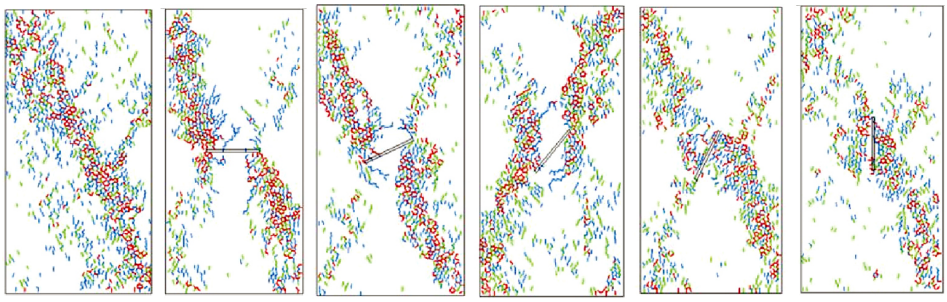

(a) Intact specimen (b) $\beta = 0°$ (c) $\beta = 30°$ (d) $\beta = 45°$ (e) $\beta = 60°$ (f) $\beta = 90°$

Fig. 21. Numerical simulation results of triaxial compression fracture of specimens under confining pressure of 10 MPa

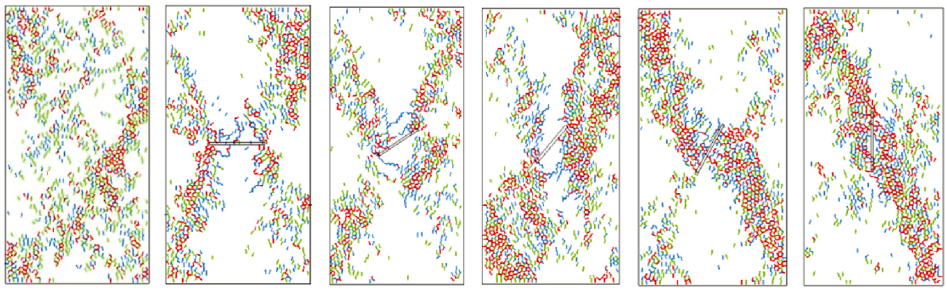

(a) Intact specimen (b) $\beta = 0°$ (c) $\beta = 30°$ (d) $\beta = 45°$ (e) $\beta = 60°$ (f) $\beta = 90°$

Fig. 22. Numerical simulation results of triaxial compression fracture of specimens under confining pressure of 15 MPa

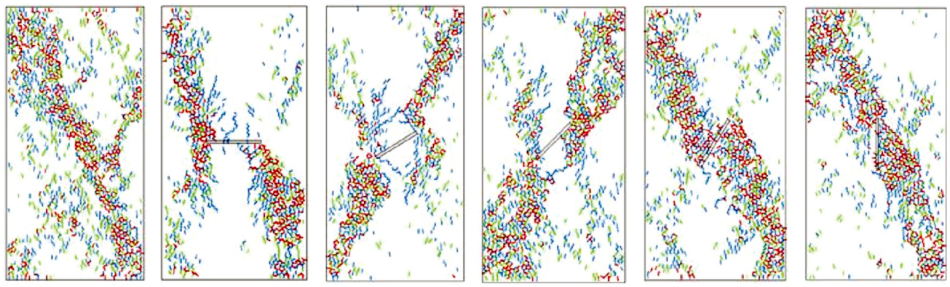

(a) Intact specimen (b) $\beta = 0°$ (c) $\beta = 30°$ (d) $\beta = 45°$ (e) $\beta = 60°$ (f) $\beta = 90°$

Fig. 23. Numerical simulation results of triaxial compression fracture of specimens under confining pressure of 10 MPa

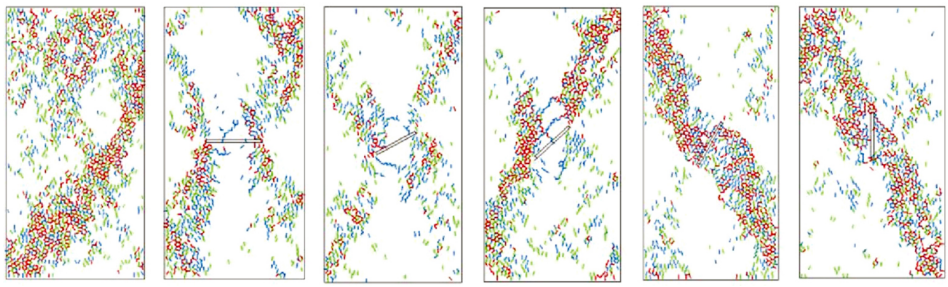

(a) Intact specimen (b) $\beta = 0°$ (c) $\beta = 30°$ (d) $\beta = 45°$ (e) $\beta = 60°$ (f) $\beta = 90°$

Fig. 24. Numerical simulation results of triaxial compression fracture of specimens under confining pressure of 15 MPa

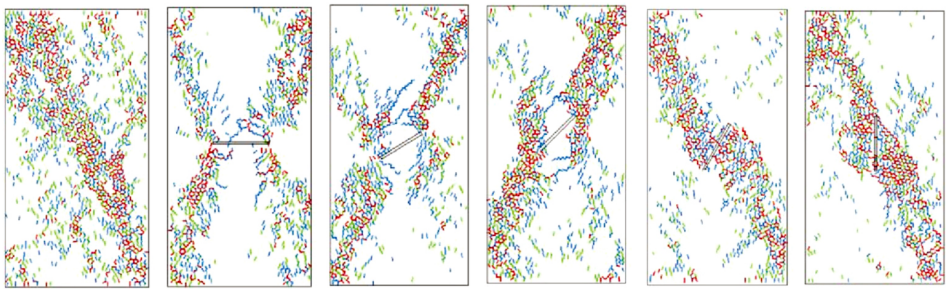

(a) Intact specimen (b) $\beta = 0°$ (c) $\beta = 30°$ (d) $\beta = 45°$ (e) $\beta = 60°$ (f) $\beta = 90°$

Fig. 25. When the initial axial stress level is 80% of the corresponding conventional triaxial compressive strength at unloading, the triaxial compression fracture of the specimen occurs

The intact specimen begins to crack along the symmetry angle direction of the specimen, and branches will be formed in the main fracture direction.

When the initial stress level is the same when unloading, with the inclined angle of prefabricated crack increasing from 0° to 90°, the more concentrated the crack distribution in the specimen, the wider the shear band formed by the crack development.

6. Conclusions

1. In case of triaxial compression, when the inclined angle of prefabricated crack increasing from 0° to 90°, the compressive strength and peak strain of the specimen increase gradually. Under the same confining pressure, the compressive strength of the intact specimen is greater than that of the specimen with cracks.
2. The compressive strength of the specimen under triaxial unloading is smaller than that under triaxial loading. The peak strain of the specimen under triaxial unloading is also smaller than that under triaxial loading. The specimen is more prone to brittle failure. When the axial stress level is the same during unloading, with the increase of the initial confining pressure during unloading, the difference of the compressive strength of the specimens with different inclined angle of prefabricated crack gradually decreases.
3. Under the condition of uniaxial compression and triaxial compression, the failure of the specimen is mainly caused by the propagation and penetration of the wing crack and the secondary crack at the tip of the prefabricated crack to form the macro section. The crack generation and penetration modes are different when the inclined angle of prefabricated crack is different. The inclined angle of prefabricated crack, loading mode and confining pressure of the prefabricated crack have influence on the fracture mode of the specimen.

Acknowledgements

This work was supported by the Open Research Fund of Hunan Provincial Key Laboratory of Hydropower Development Key Technology (Grant No. PKLHD202002), the Open Research Fund of State Key Laboratory of Geohazard Prevention and Geoenviron-

ment Protection (Grant No. SKLGP2021K020), the Open Research Fund of Engineering Research Center of Underground Mine Construction, Ministry of Education (Grant No. JYBGCZX2020101), Sichuan Science and Technology Program (No. 2019YJ0551) and Sichuan Huaxi Group Co., Ltd. (No. HXKX2020021).

References

[1] J. Chen, D. Jiang, S. Ren, et al., "Comparison of the characteristics of rock salt exposed to loading and unloading of confining pressures", *Acta Geotechnica*, vol. 11, pp. 221–230, 2016, doi: 10.1007/s11440-015-0369-9.

[2] X. L. Guo, Z. S. Tan, X. Wang, et al., "Effect of bedding angle and mineral composition on mechanical properties and fracture behavior of phyllite under unloading confining pressures", *Geotechnical and Geological Engineering*, vol. 38, pp. 3611-3621, 2020, doi: 10.1007/s10706-020-01238-0.

[3] Y. Chen, W. B. Guo, J. P. Zuo, et al., "Effect of triaxial loading and unloading on crack propagation and damage behaviors of sandstone", *Rock Mechanics and Rock Engineering*, vol. 54, pp. 6077-6090, 2021, doi: 10.1007/s00603-021-02605-w.

[4] B. Dai, G. Zhao, H. Konietzky, et al., "Experimental and numerical study on the damage evolution behaviour of granitic rock during loading and unloading", *KSCE Journal of Civil Engineering*, vol. 22, pp. 3278-3291, 2018, doi: 10.1007/s12205-018-1653-7.

[5] B. Dai, G. Zhao, H. Konietzky, et al., "Experimental investigation on damage evolution behaviour of a granitic rock under loading and unloading", *Journal of Central South University*, vol. 25, pp. 1213-1225, 2018, doi: 10.1007/s11771-018-3819-3.

[6] Y. Chen, J. Zuo, et al., "Experimental investigation on the crack propagation behaviors of sandstone under different loading and unloading conditions", *International Journal of Rock Mechanics and Mining Sciences*, vol. 130, pp. 1-10, 2020, doi: 10.1016/j.ijrmms.2020.104310.

[7] X. Huang, Q. Liu, B. Liu, et al., "Experimental study on the dilatancy and fracturing behavior of soft rock under unloading conditions", *International Journal of Civil Engineering*, vol. 15, pp. 921-948, 2017, doi: 10.1007/s40999-016-0144-9.

[8] X. Li, H. Zhao, B. Wang, and T. Xiao, "Mechanical properties of deep-buried marble material under loading and unloading tests", *Journal of Wuhan University of Technology-Materials Science Edition*, vol. 28, pp. 514-520, 2013, doi: 10.1007/s11595-013-0723-4.

[9] X. An, Y. Sun, T. Lei, et al., "Analysis of pre-peak strain energy storage transformation mechanism of diorite under triaxial loading–unloading paths", *Bulletin of Engineering Geology and the Environment*, vol. 82, no. 7, pp. 1-14, 2023, doi: 10.1007/s10064-023-03310-4.

[10] J. Dai, J.-F. Liu, L. Ran, et al., "Acoustic emission characteristics and energy evolution of salt rock for deep-salt-cavern engineering under triaxial loading and unloading", *Journal of Central South University*, vol. 30, pp. 962-974, 2023, doi: 10.1007/s11771-022-5213-4.

[11] H. Gong, Y. Luo, K. Xu, et al., "Mechanical characteristics of failure and rockburst proneness of fractured granite from Shuangjiangkou hydropower station under triaxial loading and unloading", *Bulletin of Engineering Geology and the Environment*, vol. 82, no. 7, pp. 1-19, 2023, doi: 10.1007/s10064-023-03281-6.

[12] Q.-B. Meng, J.-F. Liu, L. Ren, et al., "Experimental study on rock strength and deformation characteristics under triaxial cyclic loading and unloading conditions", *Rock Mechanics and Rock Engineering*, vol. 54, pp. 777-797, 2021, doi: 10.1007/s00603-020-02289-8.

[13] P. Yin, S. Yang, et al., "Experiment and DEM simulation study on mechanical behaviors of shale under triaxial cyclic loading and unloading conditions", *Geomechanics and Geophysics for Geo-Energy and Geo-Resources*, vol. 9, art. no. 10, 2023, doi: 10.1007/s40948-023-00554-y.

[14] X.-B. Li, Z.-H. Chen, et al., "Unloading responses of pre-flawed rock specimens under different unloading rates", *Transactions of Nonferrous Metals Society of China*, vol. 29, no. 7, pp. 1516-1526, 2019, doi: 10.1016/S1003-6326(19)65059-4.

Received: 2023-06-20, Revised: 2023-12-05